Spectrochimica Acta Part A: Molecular and Biomolecular Spectroscopy 358 (2026) 127870

Contents lists available at ScienceDirect

Spectrochimica Acta Part A:
Molecular and Biomolecular Spectroscopy

journal homepage: www.journals.elsevier.com/spectrochimica-acta-part-a-molecular-and-biomolecular-spectroscopy

Solvent-dependent photophysics of a hydroxychalcone: UV–Vis/fluorescence solvatochromism, hydrogen bonding, and computed hyper-Rayleigh first hyperpolarizability

Cristiane Alves da Fonseca E. Santo [a], Ademir J. Camargo [a], Gilberto L.B. Aquino [a], Jaqueline C. Desordi [b], Amanda G. Claudino [b], Pablo J. Gonçalves [b], Francisco A.P. Osório [b], Clodoaldo Valverde [a,c,*]

[a] Grupo de Química Teórica e Estrutural de Anápolis, Universidade Estadual de Goiás, 75001-970 Anápolis, GO, Brazil
[b] Instituto de Física, Universidade Federal de Goiás, 74.690-900 Goiânia, GO, Brazil
[c] Universidade Paulista – UNIP, 74845-090 Goiânia, GO, Brazil

HIGHLIGHTS

- HXC shows solvent-dependent UV-Vis absorption and fluorescence solvatochromism in five organic solvents.
- Methanol reveals a weak extra emission band consistent with a hydrogen-bond-stabilized charge-transfer state.
- Kamlet-Taft LSER shows solvent dipolarity/polarizability drives the Stokes-shift variation.
- Optimally tuned M11/PCM reproduces the main spectral trends and supports the photophysical assignments.
- HXC exhibits large betaHRS, strong dispersion, and pronounced resonance enhancement near 638 nm and at 1064 nm.

GRAPHICAL ABSTRACT

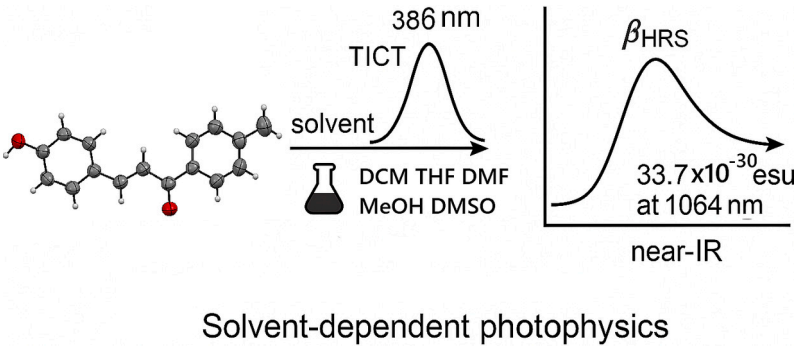

ARTICLE INFO

Keywords:
Chalcone
Nonlinear optics
Hyper-Rayleigh scattering
Absorption and emission spectra
Solvatochromism

ABSTRACT

The present work investigates the solvent-dependent optical response of the previously reported hydroxychalcone (2E)-3-(4-hydroxyphenyl)-1-(4-methylphenyl)prop-2-en-1-one (HXC). UV–Vis absorption and fluorescence spectra were recorded in five solvents of different polarity and hydrogen-bonding ability, and the solvent effects were analyzed using the Kamlet–Taft multiparameter approach. HXC shows a bathochromic shift of the main absorption band with increasing solvent polarity, while the fluorescence data reveal a reproducible broad long-wavelength emissive component in MeOH. Global deconvolution and slit-width comparison indicate that this red-shifted feature is a reproducible spectral contribution rather than a trivial instrumental artifact. Excited-state calculations further show substantial relaxation of the low-lying excited state in methanol, although the optimized S1 geometry does not support a fully developed classical TICT structure. The results therefore support the interpretation of a more strongly relaxed charge-transfer-like, TICT-like emissive state in protic methanol, while the overall solvent dependence of HXC is dominated by polarity/polarizability effects with secondary hydrogen-bonding contributions. The frequency-dependent Hyper-Rayleigh first hyperpolarizability

* Corresponding author at: Grupo de Química Teórica e Estrutural de Anápolis, Universidade Estadual de Goiás, 75001-970 Anápolis, GO, Brazil.
E-mail address: valverde@ueg.br (C. Valverde).

https://doi.org/10.1016/j.saa.2026.127870
Received 22 January 2026; Received in revised form 2 April 2026; Accepted 5 April 2026
Available online 6 April 2026
1386-1425/© 2026 Elsevier B.V. All rights are reserved, including those for text and data mining, AI training, and similar technologies.

was also computed, predicting $\beta_{HRS}(-2\omega;\omega,\omega) = 33.7 \times 10^{-30} esu$ at 1064 nm and a pronounced resonance enhancement around 638 nm. These results show that HXC behaves as a stable donor–π–acceptor chromophore with a significant second-order NLO response, especially in the near-IR.

1. Introduction

During the last years, the investigation for organic crystals that have important nonlinear optical (NLO) behaviors is getting much attention, mostly because they are used in photonic devices [1,2]. These materials are applied in high density optical storage, optical switching, signal processing [3], frequency modulators [4] transmission of data [5], and also electrochemical sensors for ultra-fast processing of optical signals [6–15]. One big advantage of the organic compounds is that they are easy to manipulate. Also, it is possible to tune the molecular NLO properties by changing the donor and acceptor strength of molecules that are linked by a π-conjugated bridge. So, to find new organic crystals that present high efficiency in nonlinear optics is a big challenge for the actual days [16–18] .

Chalcones have long attracted considerable attention due to their diverse biological activities, including antitumor, antimalarial, antimutagenic, anti-inflammatory, antimicrobial, antituberculosis, and antidiabetic properties [19–22]. In addition to their biological relevance, chalcones play a crucial role as intermediates in plant metabolic pathways and serve as versatile precursors for the synthesis of biologically active compounds [23–27].

Beyond their biological significance, increasing interest has recently been directed toward the unique physical properties of chalcones, particularly their nonlinear optical (NLO) behavior [28,29]. Chalcones have been shown to exhibit phenomena such as saturable absorption, negative refraction, optical limiting [30–34], and the generation of light with large Stokes shifts [35,36]. These features point to possible device use for the development of advanced photonic devices, including optical switches, limiters, and logic components.

Structural modifications offer an effective strategy to fine-tune the electronic distribution and bandgap of chalcones. For instance, the incorporation of ferrocenyl groups, ethynylated systems, or rigid polycyclic units has led to semiconducting materials with enhanced solubility, excellent thermal stability, and remarkable light-emitting properties [37,38]. Collectively, these advancements highlight the potential of chalcones as versatile scaffolds for the design of functional materials in optoelectronics and nonlinear photonics [39].

In this context, the present study focuses on the solution-phase photophysics and computed second-order NLO response of the previously reported hydroxychalcone (2E)-3-(4-hydroxyphenyl)-1-(4-methylphenyl)prop-2-en-1-one (HXC). HXC was previously synthesized and characterized by Costa et al. [40], including crystallographic and spectroscopic data. Therefore, the present work does not claim chemical novelty of the compound itself. Instead, our objective is to investigate how the solvent environment modulates the optical response of this already characterized donor–π–acceptor chromophore.

Because the crystal structure of HXC is centrosymmetric (P21/c), the previous study mainly addressed its solid-state structural and NLO aspects [40], whereas here we investigate its absorption, fluorescence solvatochromism, hydrogen-bonding effects, and computed frequency-dependent Hyper-Rayleigh first hyperpolarizability (β_{HRS}) in solution.

To investigate the structural features, thermal stability, and photophysical behavior of HXC, a comprehensive experimental and theoretical approach was employed. Experimental characterization involved TGA/DTG, UV–Vis spectroscopy, and fluorescence measurements in different solvents to assess thermal stability, optical properties, and solvatochromic effects. Complementarily, Density Functional Theory (DFT) calculations using the M11 functional with 6–311++G(d,p) basis set and the Polarizable Continuum Model (PCM) were conducted to explore absorption and emission spectra, NLO properties, and reactivity descriptors. Based on these results, the potential of HXC for nonlinear optical applications is discussed, considering parameters such as dipole moment, linear polarizability, and Hyper-Rayleigh scattering first-hyperpolarizability. These reports motivate a focused study of chalcones as small-molecule chromophores for optoelectronics [39].

This work presents a quantitative case study of the donor–π–acceptor chalcone HXC, combining UV–Vis absorption and fluorescence spectroscopies in dimethyl sulfoxide (DMSO), dimethyl formamide (DMF), methanol (MeOH), dichloromethane (DCM), and tetrahydrofuran (THF) with TD-DFT calculations at the M11/6–311++G(d,p)/PCM level. The main absorption band displays clear solvatochromism, shifting from 332 nm in DCM to 352 nm in DMSO. In MeOH, in addition to the local emission near 386 nm, HXC shows a reproducible broad long-wavelength emissive component, here interpreted more cautiously as arising from a more strongly relaxed charge-transfer-like, possibly TICT-like, excited state favored in the protic solvent environment [41–43]. We quantified the frequency-dependent Hyper-Rayleigh first hyperpolarizability, finding $\beta_{HRS}(-2\omega;\omega,\omega) = 33.7 \times 10^{-30}$ esu at 1064 nm and a pronounced near-resonant enhancement around 638 nm. We explicitly distinguished the Kohn–Sham orbital gap from the optical gap and provided an isospectral benchmarking (1064 nm) with p-nitroaniline and recent chalcones. This quantitative and reproducible protocol, applied to HXC, establishes a solid methodological basis for future series of D–π–A chromophores.

Although hydroxychalcone photophysics has been widely studied, the present work contributes a self-consistent dataset for a single reference chromophore obtained within the same solvent panel and the same computational framework. Specifically, we combine: (i) steady-state UV–Vis/fluorescence solvatochromism, (ii) Kamlet–Taft Linear Solvation Energy Relationship (LSER) analysis to separate general polarity from specific hydrogen-bonding contributions, and (iii) frequency-dependent β_{HRS} calculations. The goal is not to generalize to the whole class of hydroxychalcones, but to establish a clear solvent–excited-state–NLO properties correlation for HXC that can guide future series studies [42,44].

2. Experimental methods and materials

2.1. Synthesis and crystal data

The hydroxychalcone (2E)-3-(4-hydroxyphenyl)-1-(4-methylphenyl) prop-2-en-1-one (HXC) is a previously reported compound and was synthesized here following the procedure described by Costa et al. [40]. Equimolar amounts of 4-hydroxybenzaldehyde and 4-methylacetophenone were dissolved in ethanol, and aqueous KOH (20%) was added under stirring at room temperature. After 5 min, the reaction mixture was acidified to pH ≈ 3 with 4 N HCl. The precipitate was filtered, washed with water, dried, and recrystallized from ethanol to afford HXC as a yellow solid in 79% yield, mp 162.4–165.7 °C.

To make the present manuscript self-contained, the main analytical data are summarized here, consistent with the previously reported characterization [40]. ^{1}H NMR ($CDCl_3$): d 2.46 (s, 3H, C*H*$_3$Ph) 5.71 (br. s., 1H, O*H*Ph) 6.91 (d, 2H, *Ph*OH, J = 8.85 Hz) 7.32 (d, 2H, *Ph*OH, J = 7.93 Hz) 7.43 (d, 1H, CHCO, J = 15.87 Hz) 7.58 (d, 2H, PhCH$_3$, J = 8.24 Hz) 7.79 (d, 1H, CHPh, J = 15.56 Hz) 7.95 (d, 2H, PhCH$_3$, J = 8.24 Hz). ^{13}C NMR ($CDCl_3$): d 24,20 (CH_3Ph) *Ph* ring (119.51; 122.29; 130.32; 132.22; 132.94; 134.35; 149.13; 164.18) olefin. (122.29; 147.63) 194.89 (C=O); EIMS (*m/z*): 238 [M]+, 237, 223, 77. The corresponding ^{1}H NMR, ^{13}C NMR and mass spectra are provided in the Supporting Information (Figs. S1 – S4) and were used as identity/purity checks for

the isolated product.

2.2. Thermal analysis

The thermogravimetric (TGA) and derivative thermogravimetric (DTG) analyses were performed in a thermal analyzer (TGA-PYRIS 1, Perkin Elmer, USA), under a nitrogen gas (N2) atmosphere, with a flow rate of 20 mL/min, heating rate of 10 °C/min and temperature range of 25 °C to 600 °C, to evaluate the degradation of HXC. The DTG curves were obtained from the derivative of the TGA curve, recording the mass variation as function of the temperature (*dm/dT*). For the TGA analyses, approximately 1 mg of crystallized hydroxychalcone (HXC) sample was used, weighed in a platinum crucible.

2.3. Photophysical measurements

2.3.1. Sample preparation

For photophysical characterization, the hydroxychalcone crystal (HXC) was dissolved in dimethyl sulfoxide (DMSO) to obtain a 200 μM stock solution. In following, fractional dilutions from this solution were performed in DMSO in concentrations of 200 μM, 100 μM, 50 μM, 25 μM, 12.5 μM, 6.25 μM, 3.12 μM and 1.56 μM. The molar absorption coefficient (ε) of the main bands was obtained based on Lambert-Beer's Law.

2.3.2. Uv-Vis molecular absorption spectroscopy

The optical absorption spectra were carried out in several solvent media, using a UV–Vis PerkinElmer™ spectrophotometer; model Lambda 1050, available at the Biophotonics Laboratory of the Physics Institute of the Goiás Federal University (UFG). The spectra were obtained by scanning the spectral window between 255 and 500 nm, with a spectral resolution of 1 nm, through absorbance measurements of the sample solutions in a quartz cuvette with an optical path (*l*) equal to 1 cm.

2.3.3. Fluorescence spectroscopy

The fluorescence emission spectra in the solvent media were obtained using a Hitachi™ spectrofluorometer; model FL F-7000. The sample solutions had their concentration adjusted so that the absorbance at the excitation wavelength of the molecule was less than 0.1. This procedure is necessary to avoid self-absorption processes (internal filter effect), which lead to a reduction in the intensity of the emitted light detected [45]. Fluorescent emission spectra were observed through excitation at the appropriate wavelengths, with scanning speed of 240 nm/min.

3. Computational methods

All quantum chemical calculations were carried out using the Gaussian 16 software package [46]. Ground-state geometries were optimized with M11/6–311++G(d,p) using PCM (solvent according to experiment) and verified by frequency analyses. Vertical excitations were obtained via TD-DFT (M11/6–311++G(d,p), PCM). The tuning of ω (adopted value 0.145) followed the protocol detailed in the Supplementary Material; all production calculations use this value. The molecular electrostatic potential (MEP) surfaces were visualized using the Gauss View 6.0 interface. Excited-state properties in various media were obtained through time-dependent DFT (TD-DFT) calculations.

To estimate the nonlinear optical parameters of the molecule, the range-separated hybrid meta-generalized gradient approximation (meta-GGA) functional M11 was employed. This functional incorporates a position-dependent fraction of Hartree–Fock (HF) exchange, increasing from 42.8% in the short-range to 100% in the long-range. A self-consistent tuning method was used to identify the optimal range-separation parameter (ω), by minimizing the function $J(\omega)$, defined as:

$$J(\omega) = \sqrt{|\in_{HOMO}(N) + IP(N)|^2 + |\in_{HOMO}(N+1) + EA(N)|^2}. \quad (1)$$

Here, $\in_{HOMO}(N)$ and $\in_{HOMO}(N+1)$ represent the energies of the highest occupied molecular orbital (HOMO) for the neutral and anionic species, respectively. IP(N) stands for the ionization potential, and EA (N) is the electron affinity of the neutral system. The ω parameter was optimized by performing single-point energy calculations at different values ranging from 0.10 to 0.30 $bohr^{-1}$, in steps of 0.05. The value that minimized $J(\omega)$ was selected as optimal (see Fig. 1). This tuning procedure has been effectively used in previous studies to improve the accuracy of linear optical predictions for conjugated organic molecules [28] (See Table 1).

The dynamic average linear polarizability ($\langle\alpha(-\omega;\omega)\rangle$) and the total dipole moment (μ) were determined using specific mathematical expressions appropriate for each property,

$$\langle\alpha(-\omega;\omega)\rangle = \frac{1}{3}\sum_{i=x,y,z}\alpha_{ii}(-\omega;\omega), \quad (2)$$

$$\mu = \left(\mu_x^2 + \mu_y^2 + \mu_z^2\right)^{\frac{1}{2}}. \quad (3)$$

The Cartesian components of the first hyperpolarizability (β_i), along with the total magnitude (β_{tot}) and its projection along the dipole moment direction (β_{vec}), were obtained using the following mathematical relationships.

$$\beta_i(-\omega;\omega,0) = \frac{1}{3}\sum_j(\beta_{ijj} + \beta_{jji} + \beta_{jij})i,j = (x,y,z), \quad (4)$$

$$\beta_{tot}(-\omega;\omega,0) = \sqrt{\beta_x^2 + \beta_y^2 + \beta_z^2}, \quad (5)$$

and

$$\beta_{vec}(-\omega;\omega,0) = \sum_i \frac{\mu_i\ \beta_i(-\omega;\omega,0)}{|\vec{\mu}|} \quad (6)$$

When the first hyperpolarizability is aligned along the dipole direction, the projection of the first hyperpolarizability becomes equal to its total magnitude, that is, $\beta_{vec}=\beta_{tot}$. The first hyperpolarizability associated with Hyper-Rayleigh Scattering (β_{HRS}) can be defined as follows:

$$\beta_{HRS}(-2\omega;\omega,\omega) = \sqrt{\langle\beta_{ZZZ}^2\rangle + \langle\beta_{XZZ}^2\rangle}. \quad (7)$$

In this context, the laboratory coordinate system is defined by the X, Y, and Z axes. The incident light is considered to propagate along the X-axis, with its polarization aligned in the *Z*-direction. The quantities

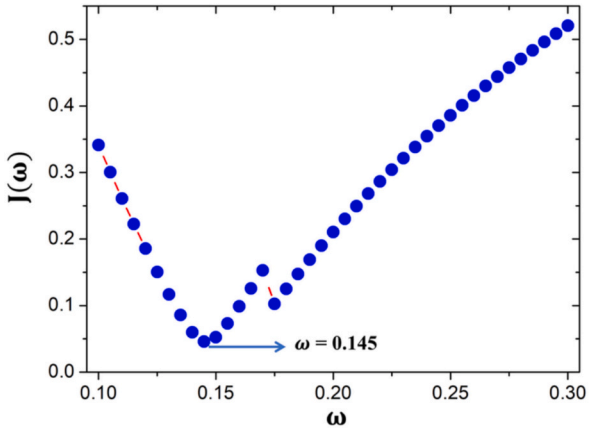

Fig. 1. Behavior of the function J(ω) as a function of the range-separation parameter. The optimal value found was ω = 0.145.

Table 1
HRS first hyperpolarizability coefficients (δ_n).

$\delta_1 = \sum_i \beta_{iii}^2$,	$\delta_2 = \sum_{i,j} \beta_{iii}\beta_{ijj}$,	$\delta_3 = \sum_{i,j} \beta_{iii}\left(\beta_{ijj} + \beta_{jji}\right)$,
$\delta_4 = \sum_{i,j} \beta_{ijj}^2$,	$\delta_5 = \sum_{i,j} \beta_{ijj}\left(\beta_{jij} + \beta_{jji}\right)$,	$\delta_6 = \sum_{i,j} \left(\beta_{jij} + \beta_{jji}\right)^2$,
$\delta_7 = \sum_{i,j,k} \beta_{ijj}\beta_{ikk}$,	$\delta_8 = \sum_{i,j,k} \left(\beta_{jij} + \beta_{jji}\right)(\beta_{kik} + \beta_{kki})$,	$\delta_9 = \sum_{i,j,k} \beta_{ijj}(\beta_{kik} + \beta_{kki})$,
$\delta_{10} = \sum_{i,j,k} \left(\beta_{ijk} + \beta_{ikj}\right)^2$,	$\delta_{11} = \sum_{i,j,k} \left(\beta_{ijk} + \beta_{ikj}\right)\left(\beta_{jjk} + \beta_{jki}\right)$.	

$\langle\beta_{ZZZ}^2\rangle$ and $\langle\beta_{XZZ}^2\rangle$ represent macroscopic averages derived from the Cartesian components of the first hyperpolarizability tensor (β_{ijk}), and are calculated using the following expressions:

$$\langle\beta_{ZZZ}^2\rangle = \frac{1}{210}(30\delta_1 + 12(\delta_2 + \delta_3 + \delta_5) + 6(\delta_4 + \delta_6) + 2(\delta_7 + \delta_8 + \delta_{11}) + 4\delta_9 + \delta_{10}), \tag{8}$$

$$\langle\beta_{XZZ}^2\rangle = \frac{1}{210}(6(\delta_1 - \delta_3 - \delta_5 + \delta_7) + 8\delta_2 + 18\delta_4 + 4\delta_6 - \delta_8 - 2\delta_9 + 3\delta_{10} - \delta_{11}), \tag{9}$$

4. Results and discussions

4.1. Thermal stability

The TGA/DTG data for HXC in crystal (see Fig. 2) reveals thermal behavior characterized by: (i) initial loss of volatile components below 150 °C (ii) decomposition onset temperature at approximately 220 °C, (iii) maximum decomposition rate at 293.4 °C, (iv) gradual stabilization above 350 °C and (v) final residue of approximately 5% at 600 °C. These results are consistent with the expected thermal behavior for substituted chalcones [47] and provide valuable information for potential applications of this compound in contexts requiring moderate thermal stability.

4.2. Solvatochromism and photophysic

The solvent panel was chosen to probe both nonspecific dielectric stabilization and specific hydrogen-bonding effects relevant to chalcone excited states. DMSO and DMF represent highly polar aprotic media; MeOH provides a polar protic environment capable of hydrogen-bond donation; and DCM and THF represent less polar aprotic solvents. This set therefore offers contrast not only in dielectric constant, but also in Kamlet–Taft parameters (π*, α, β), allowing us to distinguish general polarity effects from specific solute–solvent interactions within a compact but chemically diverse solvent series.

The UV–Vis-absorption and fluorescence spectra were performed in five organic solvents, namely: DMSO, DMF, MeOH, DCM, and THF with dielectric constant values of 46.7, 36.7, 32.7, 8.93 and 7.53, respectively. The dielectric constant value indicates the capacity of a solvent to reduce the strength of an electric field within it, and is an essential parameter for evaluating the polarity of the solvent. Higher values of dielectric constant correspond to more polar solvents.

Fig. 3 shows the absorption spectra of HXC in the evaluated solvents, which display the characteristic profile of chalcones. The main absorption band, with maxima between 332 nm and 352 nm, is attributed to the π–π* transition of the conjugated system, while the weaker band near 270 nm is assigned to Band II, a higher-energy transition characteristic of chalcones (mainly π → π*). Any possible carbonyl n → π* contribution, when present, is expected to be very weak and may appear only as an unresolved shoulder [44,48]. The band positions show solvent-dependent shifts, consistent with solvatochromic behavior in chalcone-type chromophores [49]. The maximum absorption peaks are observed at 332 nm (3.73 eV) in DCM, 342 nm (3.63 eV) in THF, 346 nm (3.58 eV) in DMF, 347 nm (3.57 eV) in MeOH, and 352 nm (3.52 eV) in DMSO. This variation corresponds to experimental optical gap energies (E_{opt}) ranging from 3.52 to 3.73 eV.

Fig. 4(a) shows the UV–Vis absorption spectra of HXC in DMSO at varying concentrations. The corresponding plot of absorbance (A) versus molar concentration (c) at 352 nm is presented in Fig. 4(b), displaying excellent linearity ($R^2 \approx 1$). According to the Beer–Lambert law, the molar absorption coefficient (ε) was determined from the slope of the linear fit of A as a function of c, where the slope corresponds to the product $\varepsilon\ell$. The calculated ε value was $\varepsilon(352\ nm) = (1.78 \pm 0.10) \times 10^4\ M^{-1}\ cm^{-1}$.

Fig. 5 illustrates the fluorescence spectra of HXC recorded in multiple solvents under excitation at 352 nm, which coincides with the maximum absorption peak observed in DMSO.

In MeOH, the fluorescence profile exhibits a reproducible broad long-wavelength emissive component under different excitation wavelengths. Importantly, the normalized spectra recorded under three slit-width conditions remain qualitatively unchanged (Fig. S5), indicating that this red-shifted feature is not a trivial slit-width artifact. A global deconvolution of the MeOH spectra (Fig. S6 and Table S16 —S17) further shows that the emission is dominated by a broad long-wavelength component centered at 447.8 nm (FWHM = 98.0 nm), together with weaker short-wavelength contributions at 389.0 and

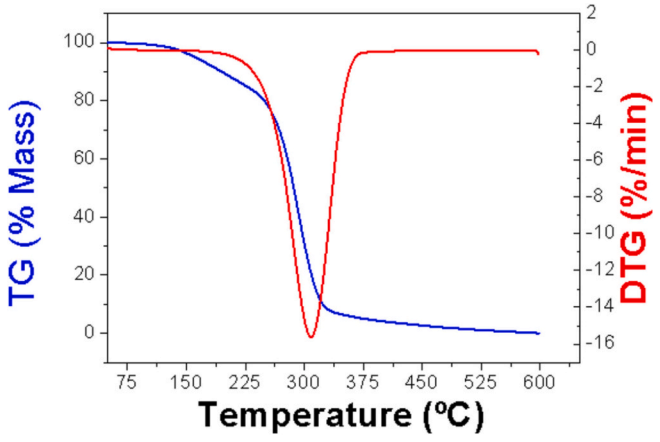

Fig. 2. TGA (Blue) and DTG (Red) thermogram for the HXC chalcone. (For interpretation of the references to colour in this figure legend, the reader is referred to the web version of this article.)

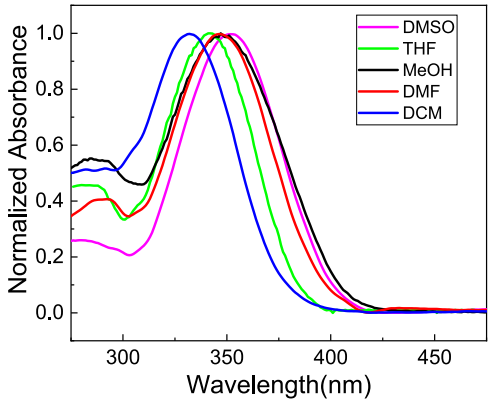

Fig. 3. Experimental UV–vis spectra at the range of 270–500 nm of HXC in several solvent media.

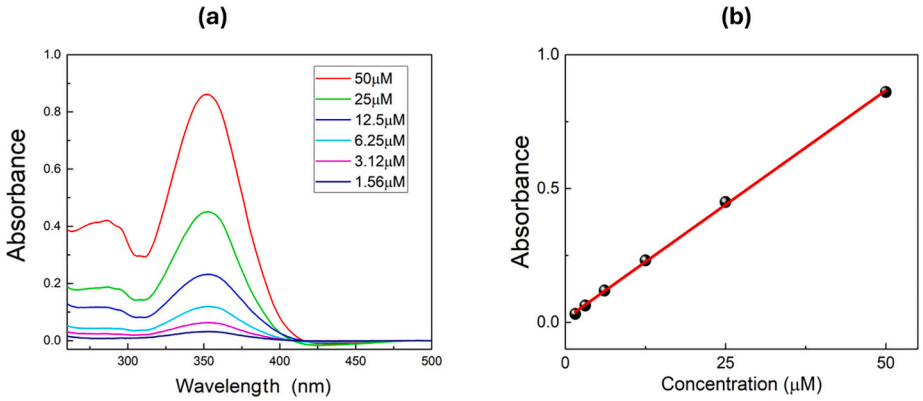

Fig. 4. (a) Concentration-dependent absorption spectra of HXC in DMSO. (b) absorbance vs concentration plot.

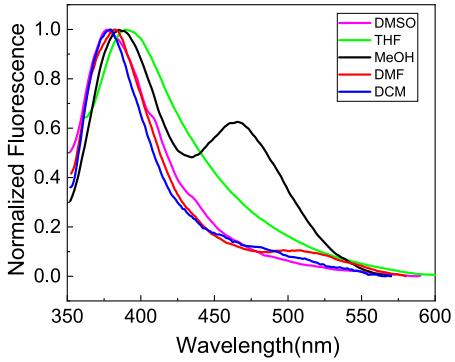

Fig. 5. Fluorescence spectra of HXC in five different solvents (excitation at 352 nm).

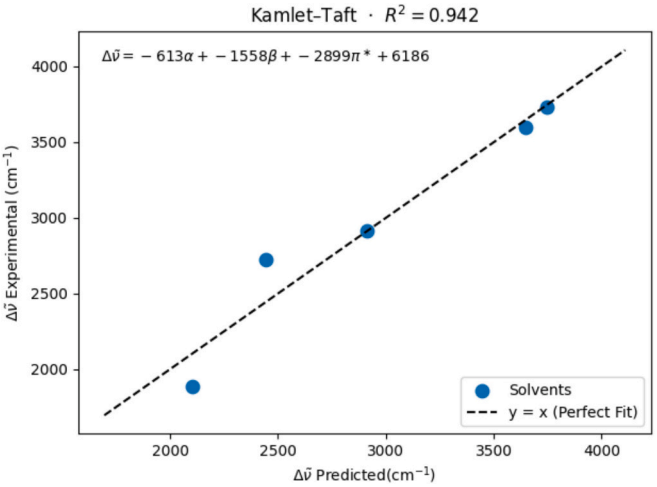

Fig. 6. The plot of the experimental Stokes shift versus the value predicted by the Kamlet-Taft multiparameter equation.

410.7 nm; in the three-peak model, the red-shifted component accounts for 96.3–98.6% of the total fitted area across the three slit settings. Excited-state optimization in MeOH also indicates substantial relaxation of the low-lying excited state relative to the vertical excitation: whereas the bright vertical absorption is dominated by a higher state, the followed low-lying state relaxes to the ~414 nm region. However, the optimized S1 geometry (Table S18) does not support a fully developed classical TICT structure. The central enone dihedral ω3 (C5–C8–C9–C10) changes only slightly from 172.99° in S0 (Table S19) to 171.28° in S1, ω1 (C4–C5–C8–O1) becomes more planar from 160.25° to 172.79°, and the largest torsional change is localized in ω2 (C16–C11–C10–C9), which decreases from 178.43° to 162.54°. Therefore, the MeOH fluorescence is more appropriately described as a reproducible broad long-wavelength emissive component associated with a more strongly relaxed charge-transfer-like, possibly TICT-like, state in protic methanol, rather than as definitive proof of a fully developed classical TICT state.

This cautious interpretation is consistent with recent chalcone literature, in which TICT assignments are supported by solvent-dependent spectroscopy together with excited-state relaxation analysis, rather than by a single spectral feature alone [50].

To place this solvent-dependent behavior on a broader quantitative basis, we applied the Kamlet–Taft multiparameter model [51] Fig. 6, is a multi-parameter Linear Solvation Energy Relationship (LSER) used to deconvolute solvent effects into distinct contributions. Unlike single-parameter models, it separates the general effects of solvent dipolarity/polarizability (π*) from specific hydrogen-bonding interactions, namely the solvent's hydrogen bond donating (HBD) ability, or acidity (α), and hydrogen bond accepting (HBA) ability, or basicity (β). The solvatochromic shift is described by the equation $\Delta\tilde{\nu} = a\alpha + b\beta + s\pi^* + \tilde{\nu}_0$, where the coefficients *s*, *a*, and *b* represent the sensitivity of the molecule's Stokes shift to each of these solvent properties.

The Kamlet–Taft regression gives a strong linear correlation, with $R^2 = 0.942$. This high R^2 value indicates that the model successfully explains over 94% of the variance in the experimental data, which is a significant improvement over the single-parameter models. The data points lie very close to the y = x line, which represents a perfect fit, visually confirming the strength of the correlation.

The resulting regression equation, $\Delta\tilde{\nu} = -613\alpha - 1558\beta - 2899\pi^* + 6186$, allows for a detailed analysis of each contribution to the Stokes shift. All three coefficients are negative, indicating that larger values of any solvent parameter reduce the Stokes shift, consistent with the increase in molecular dipole upon excitation. The dominant term is the dipolarity/polarisability parameter π^* (s = − 2899 cm^{-1}); hydrogen-bond basicity β (b = − 1558 cm^{-1}) plays a secondary role, while hydrogen-bond acidity α (a = − 613 cm^{-1}) has the smallest impact. Hydrogen bonding from protic solvents therefore modulates the shift, but general polarity remains the primary driver.

Theoretical dipole moments (μ_g = 2.29 D, μ_e = 5.14 D; $\Delta\mu$ = 2.85 D) support this interpretation: the more polar excited state is stabilised in solvents with higher π^*, mirroring the large negative coefficient for that term.

The theoretical analysis began with a small benchmark in which four density-functional schemes were tested: ωB97X-D combined with PCM, ωB97X-D combined with SMD (Solvation Model based on Density), CAM-B3LYP combined with PCM, and an individually optimized M11 combined with PCM. Among these options the optimized M11

functional reproduced the experimental absorption and fluorescence maxima most faithfully. Consequently, the discussion below is based on M11 together with the 6–311++G(d,p) basis set, whereas the complete benchmark data obtained with the other functionals have been placed in the Supporting Information. This level of theory proved to be the most suitable among the tested schemes for reproducing the experimental optical data of HXC in solution.

Table 2 collects the experimental and calculated absorption maxima, emission maxima, and Stokes shifts for HXC in five solvents of different polarity. A clear bathochromic trend appears in the experimental absorption data: the band moves from 332 nm in dichloromethane to 352 nm in DMSO. The computed wavelengths show a similar bathochromic trend, but they do not follow the exact experimental order. For instance, the experimental absorption maxima follow the order DCM < THF < DMF < MeOH< DMSO, while the calculated order is THF < DCM = MeOH < DMF=DMSO. The largest discrepancy in the absorption block occurs for DMSO (~29 nm), while the smallest is found for DCM (~11 nm) Considering the simplicity of the continuum treatment of solvents, these deviations are acceptable for conjugated organic systems.

The emission column of Table 2 shows that the fluorescence maximum shows a clear dependence on the solvent media. Among the aprotic solvents, only a modest shift of 3 nm is observed, from 379 nm in DCM to 382 nm in DMF. In methanol, the emission band appears at 386 nm, giving an experimental Stokes shift 39 nm. Hydrogen bonding between the phenolic OH group and the protic solvent (MeOH) probably stabilises the relaxed excited state more than the ground state, contributing to the moderate red shift observed. The continuum calculation model cannot capture this specific interaction, and the calculation now slightly overestimates the emission wavelength by about 1%. In the other four solvents, the error in the emission wavelength is generally small, with the largest being 3.3% for DMSO.

The Stokes shift values illustrate how strongly the excited state reorganises before emission. In the least polar solvent, THF, the experimental result for the Stokes shift is 48 nm, while in DMSO it is only 25 nm even though DMSO is more polar. The result suggests that competing factors, such as excited-state hydrogen bonding or conformational relaxation, act together with dielectric stabilization. The calculated shifts do not perfectly mirror the experimental order and tend to overestimate the gap size. In the model, the calculated Stokes shift slightly decreases from 70 nm in DCM to 67 nm in DMSO, which differs from the experimental trend. This overestimation again hints at limitations of a purely electrostatic solvent description.

Table 2
Experimental and theoretical absorption and emission maxima of HXC in different solvents, reported in wavelength (nm) and energy (eV), with relative percentage deviations calculated based on energy values.

Solvent	Abs Exp.	Abs DFT	Δ% Abs	Emis. Exp.	Emis. DFT	Δ% Emi.	Stokes Exp.
DCM	332 nm (3.73 eV)	321 nm (3.86 eV)	3.4	379 nm (3.27 eV)	391 nm (3.17 eV)	3.1	47
DMF	346 nm (3.58 eV)	323 nm (3.84 eV)	7.1	382 nm (3.25 eV)	390 nm (3.18 eV)	2.1	36
DMSO	352 nm (3.52 eV)	323 nm (3.84 eV)	9.0	377 nm (3.29 eV)	390 nm (3.18 eV)	3.3	25
THF	342 nm (3.63 eV)	320 nm (3.87 eV)	6.9	390 nm (3.18 eV)	392 nm (3.16 eV)	0.5	48
MeOH	347 nm (3.57 eV)	321 nm (3.86 eV)	8.1	386 nm (3.21 eV)	390 nm (3.18 eV)	1.0	39

4.3. Electronic structure and frontier orbitals

Table 3 refer to the standard set of global reactivity descriptors extracted from the frontier orbitals. The energy of the highest occupied molecular orbital is denoted E_{HOMO}, while E_{LUMO} represents the energy of the lowest unoccupied molecular orbital. Their separation, $\Delta\varepsilon_{KS} = E_{LUMO} - E_{HOMO}$, defines the the Kohn–Sham orbital gap (HOMO–LUMO energy gap), that is different of the optical energy gap (E_{opt}). The vertical ionization potential is approximated as $IP \approx -E_{HOMO}$, and the electron affinity as $EA \approx -E_{LUMO}$. Using these two quantities, the absolute electronegativity is calculated by $\chi_e = (IP + EA)/2$, whereas the chemical hardness is $\eta = (IP - EA)/2$; note that η is also equal to $\Delta\varepsilon_{KS}/2$ by construction. The inverse of hardness gives the chemical softness, $S = 1/\eta$. A related descriptor, the electrophilicity index, follows from $\omega_e = \chi_e^2/(2\eta)$. Finally, the negative of electronegativity defines the chemical potential, $\mu_q = -\chi$, which measures the tendency of the electron cloud to escape from the molecule.

Frontier-orbital data in Table 3 reveal that the HOMO–LUMO energy gap stays near 7.2 eV in every medium. Both HOMO and LUMO energies shift by less than 0.02 eV across the series. However, this negligible variation should not be interpreted as evidence that the intrinsic electronic structure is solvent-insensitive; rather, it reflects a known limitation of the ground-state PCM continuum model. Consequently, the Kohn–Sham gap ($\Delta\varepsilon_{KS}$) cannot be the main driver of the optical shifts discussed earlier. Instead, solvation modifies the excitation energy primarily through the differential stabilization of the ground and excited states, an effect not fully captured by static orbital energies.

Table 3 also lists several global reactivity descriptors derived from the frontier levels. Ionization potential, electron affinity, electronegativity, chemical hardness, and electrophilicity all remain constant to two decimal places, which means that the molecule keeps the same electrophilic character in every solvent. The softness S stays at 0.28 eV^{-1}, indicating a moderate ability of the electron cloud to polarise. These values suggest that, within the limits of the implicit solvation model, the fundamental ground-state reactivity remains robust. Therefore, the experimentally observed solvatochromism arises mainly from excited-state dynamics and specific interactions not reflected in these static ground-state descriptors.

While the global reactivity descriptors remain largely insensitive to the solvent, their values provide significant insight into the chemical nature of HXC. The large HOMO-LUMO energy gap of approximately 7.2 eV and the high chemical hardness ($\eta \approx 3.61$ eV) indicate that HXC is a kinetically stable molecule with low overall reactivity. However, the electrophilicity index ($\omega_e \approx 2.95$ eV) classifies HXC as a strong electrophile, suggesting a high susceptibility to accept electrons from a suitable donor.

To further elucidate the nature of the electronic transitions, we analyzed the Frontier Molecular Orbitals (FMOs). The HOMO is predominantly localized on the electron-donating hydroxyphenyl group, while the LUMO is concentrated on the electron-withdrawing propenone bridge and the methylphenyl ring. This spatial separation confirms the strong intramolecular charge transfer (ICT) character upon excitation, which is crucial for the observed NLO response. The Molecular Electrostatic Potential (MEP) map, which identifies reactive sites for electrophilic and nucleophilic attacks, is presented in Fig. S10 (Supplementary Information).

4.4. Linear and nonlinear optical properties

The last set of data, gathered in Table 4, presents the total and the Cartesian components of the HXC-dipole moment in the several solvent media. The value rises slightly from 3.35 D in THF to 3.40 D in DMSO and 3.39 D in MeOH. Although the increase is modest, it matches the rank of solvent polarity and supports the solvatochromic picture drawn from Table 2. A larger dipole stabilised by a polar solvent lowers the

Table 3
Frontier Molecular Orbital Parameters of HXC.

Solvent	E_{HOMO} (eV)	E_{LUMO} (eV)	$\Delta\varepsilon_{KS}$ (Gap) (eV)	IP (eV)	EA (eV)	χ_e (eV)	η (eV)	S (eV^{-1})	ω_e (eV)	μ_q (eV)
DCM	−8.22	−1.00	7.22	8.22	1.00	4.61	3.61	0.28	2.94	−4.61
DMF	−8.21	−1.00	7.21	8.21	1.00	4.61	3.61	0.28	2.95	−4.61
DMSO	−8.21	−1.00	7.21	8.21	1.00	4.61	3.60	0.28	2.95	−4.61
THF	−8.22	−1.00	7.22	8.22	1.00	4.61	3.61	0.28	2.94	−4.61
MeOH	−8.21	−1.00	7.21	8.21	1.00	4.61	3.61	0.28	2.95	−4.61

Table 4
Total and Cartesians components of Dipole Moment (D)of HXC in each solvent.

SOLVENT	μ_x	μ_y	μ_z	μ(D)
DCM	1.17	−2.75	−1.52	3.36
DMF	1.18	−2.79	−1.53	3.39
DMSO	1.19	−2.79	−1.53	3.40
THF	1.16	−2.74	−1.52	3.35
MeOH	1.18	−2.79	−1.53	3.39

energy of the excited state relative to the ground state, leading to the observed bathochromic shifts.

The decomposition of the dipole moment into its Cartesian components shows that the resulting vector is anchored mainly along the negative y axis, which has the largest contribution in magnitude ($|\mu_y| \approx$ 2.79 D), followed by the negative z axis and, in smaller degree, the positive x axis. The constancy of the proportions between μ_x, μ_y, and μ_z across the different media confirms that the solvent polarity intensifies the charge separation (increasing the total magnitude), but it preserves the original vector orientation of the molecule in the ground state. The dipole moment vector and the Cartesian axes are shown in Fig. S12 of the Supporting Information (SI).

The three tables outline a coherent scenario. Optical bands move to lower energy with increasing solvent polarity. The small rise in dipole moment and the special role of hydrogen bonding in methanol complete the picture. Together these findings show that HXC possesses a robust electronic core that responds to its environment mainly by adjusting transition energies rather than by changing its intrinsic electronic structure. Table 5 shows the average linear polarizability, for HXC in five solvents and at several excitation wavelengths.

The static α-value lies near $42 \times 10^{-24} esu$ for every solvent medium, confirming that solvent polarity alone has little influence on the size of the p-electron cloud. When frequency is introduced, the polarizability first drops to about $36 \times 10^{-24} esu$ at 15 μm, then rises steadily as the wavelength shortens. It reaches roughly $54 \times 10^{-24} esu$ at 400 nm, which is close to the low-energy tail of the absorption band. This frequency-dependent profile is typical for conjugated chromophores. In SOS-type expressions for β (and β_{HRS}), the frequency dependence appears through energy denominators together with damping (finite linewidth). In the off-resonant regime the response is dominated by virtual transitions; as the photon energy approaches an allowed electronic transition, β (or β_{HRS}) may increase, but damping prevents an unphysical divergence. The parallel traces in all solvents indicate that local-field factors are nearly constant, so the frequency term governs the trend.

At long wavelength the $\beta_{||z}(-2\omega;\omega, \omega)$-values are negative and modest in size, around $-19 \times 10^{-30} esu$, again with minimal solvent dependence, see Table 6.

As the frequency increases the $\beta_{||z}(-2\omega;\omega, \omega)$-magnitude grows; near 700 nm it reaches -180×10^{-30} esu. A pronounced sign reversal then occurs close to 638 nm, where the value jumps to over $2,623 \times 10^{-30} esu$ in dichloromethane and to values slightly lower but comparable figures in the other solvent media. Such an abrupt change signals a two-photon resonance that enhances the second-order response and flips its phase. Moving deeper into the visible the hyperpolarizability values falls back to the $10^2 \times 10^{-30} esu$ range and even becomes negative again near 400 nm, except in THF where a local-field correction keeps the positive sign.

The linear polarizability is driven mainly by the proximity of electronic transitions, while $\beta_{||z}(-2\omega;\omega, \omega)$ is additionally sensitive to phase changes that arise when a two-photon energy matches the first allowed excitation. Solvent effects remain secondary for both properties, confirming that the electronic core of HXC is robust across the polarity range investigated.

A careful inspection of Table 7 reveals that the Hyper-Rayleigh-scattering first hyperpolarizability $\beta_{HRS}(-2\omega;\omega,\omega)$ is always positive and follows a clear frequency-dependent profile.

At the static limit the β_{HRS}-value is about $24 \times 10^{-30} esu$ in every solvent, which indicates only modest ground-state solvation effects. Moving into the very far-infrared (15 μm) β_{HRS} decreases slightly to roughly $18 \times 10^{-30} esu$; this reduction is expected because the virtual excitation pathways become less efficient as the photon energy approaches zero.

From 5000 nm down to 1900 nm the values begin to climb, reaching around $21 \times 10^{-30} esu$. The trend accelerates between 1500 nm and 1064 nm, where $\beta_{HRS}(-2\omega;\omega,\omega)$ grows from $24 \times 10^{-30} esu$ to about $33 \times 10^{-30} esu$. This monotonic increase is consistent with the two-state

Table 5
Average linear polarizability-values (α (10^{-24} esu)) for HXC in five solvents and at several excitation wavelengths (nm).

α (10^{-24} esu)	DCM	DMF	DMSO	THF	MeOH
∞(**static**)	41.90	41.94	41.94	41.89	41.93
15,187.8	36.73	36.76	36.76	36.72	36.76
5000	36.77	36.80	36.81	36.76	36.80
3000	36.86	36.89	36.90	36.85	36.89
1900	37.08	37.11	37.11	37.07	37.11
1500	37.30	37.34	37.34	37.29	37.33
1300	37.50	37.54	37.54	37.49	37.54
1064	37.92	37.95	37.96	37.91	37.95
900	38.44	38.48	38.49	38.43	38.48
800	38.97	39.01	39.01	38.96	39.01
700	39.79	39.84	39.84	39.78	39.84
638	40.58	40.63	40.63	40.56	40.63
532	42.99	43.06	43.07	42.98	43.06
450	47.45	47.56	47.57	47.43	47.56
400	54.35	54.55	54.57	54.30	54.54

Table 6
First hyperpolarizability component along the molecular z-axis, $\beta_{//z}(-2\omega;\omega, \omega)$ ($10^{-30} esu$), at several electric field wavelength (nm).

wavelength (nm)	DCM	DMF	DMSO	THF	MeOH
15,187.8	−19.06	−19.24	−19.26	−19.01	−19.24
5000	−19.47	−19.65	−19.67	−19.42	−19.65
3000	−20.31	−20.51	−20.53	−20.26	−20.51
1900	−22.54	−22.77	−22.79	−22.48	−22.76
1500	−25.21	−25.47	−25.49	−25.14	−25.46
1300	−28.00	−28.31	−28.33	−27.92	−28.30
1064	−35.27	−35.69	−35.72	−35.16	−35.68
900	−49.22	−49.89	−49.94	−49.05	−49.87
800	−73.38	−74.60	−74.70	−73.08	−74.56
700	−179.44	−184.60	−185.02	−178.14	−184.44
638	2626.03	2127.59	2097.28	2791.88	2144.40
532	134.22	136.88	137.10	133.57	136.78
450	113.86	115.61	115.92	113.62	115.74
400	−113.54	−118.71	−120.06	405.33	−118.93

Table 7
Hyper-Rayleigh-scattering first hyperpolarizability $\beta_{HRS}(-2\omega;\omega,\omega)$ (10^{-30} esu) of HXC in five solvents, at several radiation wavelength (nm).

wavelength (nm)	DCM	DMF	DMSO	THF	MeOh
∞(**static**)	24.53	24.71	24.72	24.48	24.70
15,187.8	17.76	17.87	17.88	17.73	17.86
5000	18.14	18.26	18.27	18.11	18.25
3000	18.95	19.07	19.08	18.92	19.07
1900	21.07	21.21	21.22	21.03	21.21
1500	23.63	23.80	23.81	23.59	23.79
1300	26.32	26.52	26.54	26.27	26.51
1064	33.41	33.68	33.70	33.34	33.67
900	47.21	47.67	47.71	47.09	47.65
800	71.60	72.50	72.57	71.38	72.46
700	181.40	185.84	186.20	180.28	185.69
638	2817.54	2272.64	2239.37	2999.00	2290.60
532	308.91	318.06	318.80	306.75	317.58
450	337.18	328.64	327.91	340.06	328.62
400	355.51	350.54	350.90	532.59	350.16

approximation in which β scales roughly with $\mu^2/\Delta E^3$; as the excitation energy approaches half of the lowest allowed electronic transition the denominator shrinks and the nonlinear response intensifies.

An increase is observed between 900 nm and 638 nm. At 800 nm $\beta_{HRS}(-2\omega;\omega,\omega)$ is already near $72 \times 10^{-30} esu$, and at 700 nm it jumps to about $185 \times 10^{-30} esu$. The true peak occurs at 638 nm, where the coefficient soars above $2,200 \times 10^{-30} esu$, with the exact amplitude depending slightly on the solvent. This giant response coincides with the two-photon resonance condition $2\omega \approx \omega_{abs}$, since Table 2 places the one-photon absorption band near 332–352 nm. The resonance sharpness confirms that HXC has a strong charge-transfer character that couples efficiently to an external optical field when the virtual denominator in the sum-over-states expression approaches zero.

Beyond the resonance the coefficient drops but remains sizeable. At 532 nm $\beta_{HRS}(-2\omega;\omega,\omega)$ is still about $310 \times 10^{-30} esu$, and it stabilises near $(340 - 360) \times 10^{-30} esu$ in the 450–400 nm region. The shoulder at 400 nm, especially the larger value in THF, suggests the onset of a single-photon contribution as the excitation energy begins to overlap the lowest allowed transition.

Solvent polarity modulates the magnitude but not the overall shape of the dispersion curve. The effect is modest in the non-resonant regions, but it becomes significant at the peak of the resonance. For example, at 638 nm, the calculated β_{HRS} value in THF is over 30% larger than the value in DMSO, showing that local-field factors can notably scale the peak height. This limited sensitivity reflects the small solvent-induced changes in permanent dipole moment (Table 4) and the essentially constant HOMO–LUMO energy gap (Table 3). Local-field factors therefore dominate the solvent effect, shifting the resonance slightly without altering the fundamental electronic response of the chromophore.

Overall, we find three practical points. First, HXC offers its strongest second-order response in the near-infrared window around 638 nm. Second, the response remains robust when the molecule is transferred from non-polar to moderately polar solvents, so polymer hosts of similar polarity should preserve its performance. Third, the sharp spectral profile makes HXC a promising candidate for wavelength-selective optical switching, frequency conversion or bio-imaging applications where a high $\beta_{HRS}(-2\omega;\omega,\omega)$ at telecom-relevant or tissue-friendly wavelengths is desirable.

We use p-nitroaniline (pNA) as a common HRS benchmark. At 1064 nm, the computed β_{HRS} of HXC is $33.70 \times 10^{-30} esu$ in DMSO and $33.67 \times 10^{-30} esu$ in MeOH, while the reference pNA values reported in the same media are $24.3 \times 10^{-30} esu$ (DMSO) and $24.8 \times 10^{-30} esu$ (MeOH) [52]. This comparison is intended as an order-of-magnitude benchmark, since β_{HRS} values depend on methodology (electronic-structure level and solvation treatment) and HRS-type measurements may present non-negligible uncertainties (e.g., concentration and laser-power fluctuations) [44]. Furthermore, the β_{HRS} of HXC is larger than values reported for other chalcone derivatives at 1064 nm [53,54], supporting that HXC lies at the high end of the reported range for chalcone-based chromophores. Importantly, the β_{HRS} dispersion of HXC shows a pronounced resonance enhancement around ~638 nm, which is a key feature for wavelength-selective second-order NLO response [44].

4.4.1. *Analysis of the first hyperpolarizability 3D dispersion map*

To provide a comprehensive overview of the second-order NLO phenomena, the first hyperpolarizability tensor component, β(−(ω1 + ω2);ω1,ω2), was calculated as a function of two incident optical frequencies, ω1 and ω2. The resulting 3D dispersion map visualizes various NLO processes, including Sum Frequency Generation (SFG), Second Harmonic Generation (SHG), Electro-optic Pockels Effect (EOPE), and Optical Rectification (OR).

Fig. 7 displays the 3D dispersion map of the first hyperpolarizability (β) for the HXC molecule. The plot reveals several distinct features corresponding to important NLO processes. The z-axis, representing the magnitude of β, shows extremely large positive and negative values, indicating a strong NLO response under specific frequency conditions.

A prominent feature of the map is the series of intense, sharp peaks observed along the diagonal where ω1 = ω2. According to the established interpretation, these peaks indicate a strong Second Harmonic Generation (SHG) effect. This finding is consistent with the large resonant peak observed for the β_{HRS} value at 638 nm (0.072 a.u.). The intense peaks along the diagonal indicate a strong Second Harmonic Generation (SHG) effect, which is expected, as Hyper-Rayleigh scattering is an incoherent second-harmonic generation process where SHG is the primary contributor to the measured signal.

Furthermore, significant peaks with large amplitudes are present along the axes where either ω1 = 0 or ω2 = 0. These features are a clear signature of a large Electro-optic Pockels Effect (EOPE). This suggests that the refractive index of a material containing HXC could be effectively modulated by applying a static or low-frequency electric field, which is a key property for electro-optic devices.

Another set of sharp peaks is visible along the anti-diagonal, where ω1 = −ω2. This indicates a notable Optical Rectification (OR) effect, which is the generation of a DC polarization in the material in response to an intense optical field. The concentration of the largest β values along these specific axes and diagonals reveals that SHG, EOPE, and OR are the dominant second-order NLO phenomena for the HXC molecule. The rest of the surface, representing general Sum and Difference Frequency Generation, shows a comparatively smaller response. This

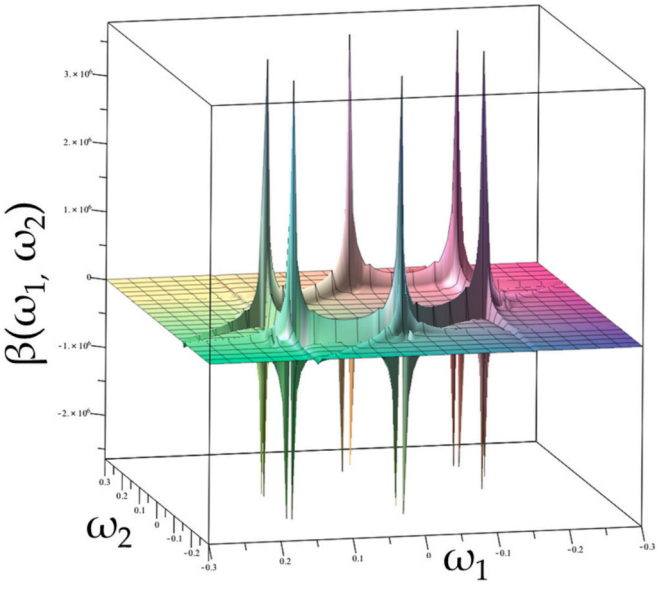

Fig. 7. Frequency-dependent first hyperpolarizability surface β(ω₁, ω₂) [a.u.]

detailed frequency-dependent analysis further highlights the potential of HXC for various NLO applications, such as frequency conversion (SHG) and electro-optic modulation (EOPE).

4.5. Potential applications

The crystal structure reported for HXC [40] is centrosymmetric ($P2_1/c$); therefore, the first hyperpolarizability and the second-order susceptibility ($\chi^{(2)}$) are zero by symmetry. Our study reports the molecular Hyper-Rayleigh scattering (HRS) first hyperpolarizability in solution. In practice, chromophores characterized in solution are subsequently used in a series of application platforms: (i) electric-field poled polymer films, employed in integrated electro-optic modulators, frequency doubling, and wavelength conversion [55]; (ii) guest–host systems, where molecules with high are dispersed in glass or polymer matrices for integrated photonics devices [56]; (iii) self-assembled monolayers and Langmuir–Blodgett films, explored in second-harmonic generation studies at interfaces [57]; (iv) hybrid and supramolecular materials, such as organic–inorganic complexes and organized aggregates, where molecular oriented in non-centrosymmetric networks results in effective [58]; and (v) NLO probes for bioimaging, where chromophores with strong charge transfer and high are designed for second-harmonic microscopy or Hyper-Rayleigh scattering in biomolecular environments [59]. In this context, the measured for HXC positions this chalcone as a natural candidate for integration into poled films and guest–host systems.

5. Conclusion

In this study, the photophysical and nonlinear optical (NLO) properties of the chalcone HXC were characterized through a combination of experimental measurements and theoretical calculations. The experimental solvatochromic study demonstrated how the absorption and emission energies of HXC are influenced by the solvent medium, with a notable effect from hydrogen bonding in protic media. Theoretical calculations performed with an optimally tuned M11 functional provided results that were with the experimental data and offered deeper insight into the molecule's electronic structure.

The analysis of global reactivity descriptors, such as the HOMO-LUMO energy gap and chemical hardness, indicated that HXC possesses a stable electronic core. The Molecular Electrostatic Potential (MEP) map identified the carbonyl oxygen and the phenolic proton as the most reactive sites for electrophilic and nucleophilic interactions, respectively. The central finding of this work is the large Hyper-Rayleigh-scattering first hyperpolarizability (β_{HRS}) of HXC, which shows a strong resonance enhancement around 638 nm. At 1064 nm, the computed β_{HRS} of HXC is competitive with the p-nitroaniline (pNA) benchmark [44]. This large NLO response, originating from its donor-π-acceptor structure, indicates that HXC is suitable for studies aimed at second-order processes near 638 nm and 1064 nm. Future work could focus on synthesizing derivatives of HXC to further modulate these properties for specific device requirements.

The present conclusions are restricted to HXC within the investigated solvents and conditions. A systematic series of related hydroxychalcones will be studied in future work to establish broader structure–property correlations [44].

Contribution

All authors contributed to the study conception and design. The experiments were carried out by C.A.F.E.S, A.J.C., G.L.B.A., P.J.G., F.A.P.O., and C.V. The theoretical calculations were performed by C.A.F.E.S, A.J.C., P.J.G., F.A.P.O., and C.V. The first draft of the manuscript was written by C.A.F.E.S, A.J.C., G.L.B.A., P.J.G., F.A.P.O., and C.V.. And all authors commented on previous versions of the manuscript. All authors read and approved the final manuscript.

Declaration of competing interest

The authors declare that they have no known competing financial interests or personal relationships that could have appeared to influence the work reported in this paper.

Acknowledgments

The authors would like to thank the following Brazilian agencies for financial support: Conselho Nacional de Desenvolvimento Científico e Tecnológico (CNPq), Coordenação de Aperfeiçoamento Pessoal de Nível Superior (CAPES) and Fundação de Apoio à Pesquisa do Estado de Goiás (FAPEG) e ao LAMCAD UFG.

Appendix A. Supplementary data

Supplementary data to this article can be found online at https://doi.org/10.1016/j.saa.2026.127870.

Data availability

No data was used for the research described in the article.

References

[1] L. Lu, Z. Liang, L. Wu, Y. Chen, Y. Song, S.C. Dhanabalan, J.S. Ponraj, B. Dong, Y. Xiang, Few-layer bismuthene: sonochemical exfoliation, nonlinear optics and applications for ultrafast photonics with enhanced stability, Laser & Photonics Reviews 1700221 (2017) 1–10, https://doi.org/10.1002/lpor.201700221.
[2] R. Salvi, C. Cerqueira-coutinho, E. Ricci-junior, N. Santos, S.R. Pinto, E. S. Bernardes, P. Lopes, B. De Araujo, R. Santos-oliveira, R. Salvi, C. Cerqueira-coutinho, E. Ricci-junior, N. Santos, S.R. Pinto, E.S. Bernardes, P. Lopes, Diagnosing lung cancer using etoposide microparticles labeled with ^{99m}Tc, Artif. Cells Nanomed. Biotechnol. (2017) 1401, https://doi.org/10.1080/21691401.2017.1307848.
[3] K. Wu, S. Pan, A review on structure-performance relationship toward the optimal design of infrared nonlinear optical materials with balanced performances, Coord. Chem. Rev. 377 (2018) 191–208, https://doi.org/10.1016/j.ccr.2018.09.002.
[4] G. Shi, Y. Wang, F. Zhang, B. Zhang, Z. Yang, X. Hou, Finding the next deep-ultraviolet nonlinear optical material, 2017, pp. 8–11, https://doi.org/10.1021/jacs.7b05943.
[5] A.N. Castro, L.R. Almeida, M.M. Anjos, G.R. Oliveira, H.B. Napolitano, C. Valverde, B. Baseia, Theoretical study on the third-order nonlinear optical properties and structural characterization of 3-Acetyl-6-Bromocoumarin, Chem. Phys. Lett. 653 (2016) 122–130, https://doi.org/10.1016/j.cplett.2016.04.070.
[6] I. Sheikhshoaie, W. Fabian, Quantum chemical study on the electronic structure and second-order nonlinear optical properties of salen-type schiff bases, Dyes Pigments 70 (2006) 91–98, https://doi.org/10.1016/j.dyepig.2005.04.011.
[7] A. Iwan, D. Sek, Polymers with triphenylamine units: photonic and electroactive materials, Prog. Polym. Sci. 36 (2011) 1277–1325, https://doi.org/10.1016/j.progpolymsci.2011.05.001.
[8] H.-J. Niu, Y.-D. Huang, X.-D. Bai, X. Li, Novel poly-Schiff bases containing 4,4′-diamino-triphenylamine as hole transport material for organic electronic device, Mater. Lett. 58 (2004) 2979–2983, https://doi.org/10.1016/j.matlet.2004.05.007.
[9] L.-Y. Kong, Z.-W. Li, T. Okamura, G.-H. Ma, Q. Chu, H.-F. Zhu, S.-H. Tang, W.-Y. Sun, N. Ueyama, Synthesis, structure and optical limiting property of CoII, MnII and CdII complexes with di-Schiff base and reduced di-Schiff base ligands, Chem. Phys. Lett. 416 (2005) 176–181, https://doi.org/10.1016/j.cplett.2005.09.074.
[10] İ. Kaya, M. Yıldırım, A. Avcı, Synthesis and characterization of fluorescent polyphenol species derived from methyl substituted aminopyridine based schiff bases: the effect of substituent position on optical, electrical, electrochemical, and fluorescence properties, Synth. Met. 160 (2010) 911–920, https://doi.org/10.1016/j.synthmet.2010.01.044.
[11] A.L. Briseno, S.C.B. Mannsfeld, C. Reese, J.M. Hancock, Y. Xiong, S.A. Jenekhe, Z. Bao, Y. Xia, Perylenediimide nanowires and their use in fabricating field-effect transistors and complementary inverters, Nano Lett. 7 (2007) 2847–2853, https://doi.org/10.1021/nl071495u.
[12] L. Tan, W. Jiang, L. Jiang, S. Jiang, Z. Wang, S. Yan, W. Hu, Single crystalline microribbons of perylo[1,12-b,c,d]selenophene for high performance transistors, Appl. Phys. Lett. 94 (2009) 153306, https://doi.org/10.1063/1.3120769.
[13] M. Jazbinsek, L. Mutter, P. Gunter, Photonic applications with the organic nonlinear optical crystal DAST, IEEE J. Sel. Top. Quantum Electron. 14 (2008) 1298–1311, https://doi.org/10.1109/JSTQE.2008.921407.
[14] C. Polisseni, K.D. Major, S. Boissier, S. Grandi, A.S. Clark, E.A. Hinds, Stable, single-photon emitter in a thin organic crystal for application to quantum-photonic devices, Opt. Express 24 (2016) 5615, https://doi.org/10.1364/OE.24.005615.

[15] L. Zhang, E. Pavlica, X. Zhong, F. Liscio, S. Li, G. Bratina, E. Orgiu, P. Samorì, Fast-response photonic device based on organic-crystal heterojunctions assembled into a vertical-yet-open asymmetric architecture, Adv. Mater. 29 (2017) 1605760, https://doi.org/10.1002/adma.201605760.
[16] W. Sun, M.M. McKerns, C.M. Lawson, G.M. Gray, C.-L. Zhan, D.-Y. Wang, Solvent Effect on the Third-Order Nonlinearity and Optical Limiting Ability of a Stilbazolium-like Dye, in, 2000, p. 280, https://doi.org/10.1117/12.408515.
[17] T.W. Bell, A.T. Papoulie, Angew. Chem., Int. Ed. 31 (6) (1992) 749–751.
[18] J. Safari, S. Gandomi-Ravandi, Structure, synthesis and application of azines: a historical perspective, RSC Adv. 4 (2014) 46224–46249, https://doi.org/10.1039/C4RA04870A.
[19] M. Rayees Ahmad, V. Girija Sastry, N. Bano, S. Anwar, Synthesis of novel chalcone derivatives by conventional and microwave irradiation methods and their pharmacological activities, Arabian Journal of Chemistry 9 (2016) S931–S935, https://doi.org/10.1016/j.arabjc.2011.09.002.
[20] J. Peng, A.L. Risinger, C. Da, G.A. Fest, G.E. Kellogg, S.L. Mooberry, Structure–Activity Relationships of Retro-dihydrochalcones Isolated from Tacca sp. J. Nat. Prod. 76 (2013) 2189–2194, https://doi.org/10.1021/np4005085.
[21] S.K. Awasthi, N. Mishra, B. Kumar, M. Sharma, A. Bhattacharya, L.C. Mishra, V. K. Bhasin, Potent antimalarial activity of newly synthesized substituted chalcone analogs in vitro, Med. Chem. Res. 18 (2009) 407–420, https://doi.org/10.1007/s00044-008-9137-9.
[22] A. Rampa, M. Bartolini, L. Pruccoli, M. Naldi, I. Iriepa, I. Moraleda, F. Belluti, S. Gobbi, A. Tarozzi, A. Bisi, Exploiting the chalcone scaffold to develop multifunctional agents for alzheimers disease, Molecules 23 (2018) 1902, https://doi.org/10.3390/molecules23081902.
[23] D.C. da S. Lima, C.R. do Vale, J.H. Véras, A. Bernardes, C.N. Pérez, L. Chen-Chen, Absence of genotoxic effects of the chalcone (e)-1-(2-hydroxyphenyl)-3-(4-methylphenyl)-prop-2-en-1-one and its potential chemoprevention against DNA damage using in vitro and in vivo assays, PloS One 12 (2017) e0171224, https://doi.org/10.1371/journal.pone.0171224.
[24] Y. Zheng, X. Wang, S. Gao, M. Ma, G. Ren, H. Liu, X. Chen, Synthesis and antifungal activity of chalcone derivatives, Nat. Prod. Res. 29 (2015) 1804–1810, https://doi.org/10.1080/14786419.2015.1007973.
[25] C. Zhuang, W. Zhang, C. Sheng, W. Zhang, C. Xing, Z. Miao, Chalcone: a privileged structure in medicinal chemistry, Chem. Rev. 117 (2017) 7762–7810, https://doi.org/10.1021/acs.chemrev.7b00020.
[26] L.O. Sallum, H.B. Napolitano, P. de S. Carvalho, A.F. Cidade, G.L.B. de Aquino, N. D. Coutinho, A.J. Camargo, J. Ellena, H.C.B. de Oliveira, V.H.C. Silva, Effect of the methanol molecule on the stabilization of c 18 h 18 o 4 crystal: combined theoretical and structural investigation, J. Phys. Chem. A 118 (2014) 10048–10056, https://doi.org/10.1021/jp504288r.
[27] P.S. Carvalho-Jr, L.O. Sallum, A.F. Cidade, G.L.B. Aquino, H.B. Napolitano, (E)-1-(4-methoxyphenyl)-3-(3,4,5- trimethoxyphenyl)prop-2-en-1-one, Acta Crystallogr. Sect. E Struct. Rep. Online E67 (2011) 0–7, https://doi.org/10.1107/S1600536811028984.
[28] P.S. Carvalho, J.M.F. Custodio, W.F. Vaz, C.C. Cirilo, A.F. Cidade, G.L.B. Aquino, D. M.B. Campos, P. Cravo, C.J. Coelho, S.S. Oliveira, A.J. Camargo, H.B. Napolitano, Conformation analysis of a novel fluorinated chalcone, J. Mol. Model. 23 (2017), https://doi.org/10.1007/s00894-017-3245-8.
[29] J.M.F. Custodio, E.C.M. Faria, L.O. Sallum, V.S. Duarte, W.F. Vaz, G.L.B. De Aquino, P.S. Carvalho, H.B. Napolitano, The influence of methoxy and ethoxy groups on supramolecular arrangement of two methoxy-chalcones, J. Braz. Chem. Soc. 28 (2017), https://doi.org/10.21577/0103-5053.20170067.
[30] J.M.F. Custodio, F.G. Santos, W.F. Vaz, C.E.P. Cunha, R.G. Silveira, M.M. Anjos, C. E.M. Campos, G.R. Oliveira, F.T. Martins, C.C. da Silva, C. Valverde, B. Baseia, H. B. Napolitano, Molecular structure of hybrid imino-chalcone in the solid state: X-ray diffraction, spectroscopy study and third-order nonlinear optical properties, J. Mol. Struct. 1157 (2018) 210–221, https://doi.org/10.1016/j.molstruc.2017.12.023.
[31] G.C. Ribeiro, L.R. Almeida, H.B. Napolitano, C. Valverde, B. Baseia, Polarization effects on the third-order nonlinear optical properties of two polymorphs of enamine derivative, Theor. Chem. Accounts 135 (2016), https://doi.org/10.1007/s00214-016-1999-1.
[32] I.N. Ribeiro, R.L.G. de Paula, P.R.S. Wenceslau, F.S. Fernandes, V.S. Duarte, W. F. Vaz, G.R. Oliveira, C. Valverde, H.B. Napolitano, B. Baseia, Growth and characterization of a new chlorine substituted chalcone: a third order nonlinear optical material, J. Mol. Struct. 1201 (2020), https://doi.org/10.1016/j.molstruc.2019.127137.
[33] J.M.F. Custodio, C.A. Moreira, C. Valverde, G.L.B. De Aquino, B. Baseiaa, H. B. Napolitano, Hirshfeld surfaces and nonlinear optics on two conformers of a heterocyclic chalcone, J. Braz. Chem. Soc. 29 (2018) 258–268, https://doi.org/10.21577/0103-5053.20170136.
[34] J.M.F. Custodio, J.J.A. Guimarães-Neto, R. Awad, J.E. Queiroz, G.M.V. Verde, M. Mottin, B.J. Neves, C.H. Andrade, G.L.B. Aquino, C. Valverde, F.A.P. Osório, B. Baseia, H.B. Napolitano, Molecular modelling and optical properties of a novel fluorinated chalcone, Arab. J. Chem. 13 (2020) 3362–3371, https://doi.org/10.1016/j.arabjc.2018.11.010.
[35] X. Wu, Y. Shi, Y. Ju, J. Jia, Y. Fang, Y. Chen, Q. Wu, Y. Song, Investigation of the intensity dependent transition from saturable absorption to reverse saturable absorption and ultrafast negative refraction in terthiophene-based chalcone derivatives, Opt. Mater. (Amst). 117 (2021) 111174, https://doi.org/10.1016/j.optmat.2021.111174.
[36] W.M. Khairul, F. Hashim, R. Rahamathullah, M. Mohammed, S. Aisyah Razali, S. Ahmad Tajudin Tuan Johari, S. Azizan, Exploring ethynyl-based chalcones as green semiconductor materials for optical limiting interests, Spectrochim. Acta A Mol. Biomol. Spectrosc. 308 (2024) 123776, https://doi.org/10.1016/j.saa.2023.123776.
[37] O.J. Hernández-Ortiz, J.E. Cerón-Castelán, F.M. Muñoz-Pérez, V. Salazar-Pereda, J. G. Ortega-Mendoza, M.A. Veloz-Rodríguez, A. Lobo-Guerrero, A. Espinosa-Roa, M. A. Rodríguez-Rivera, R.A. Vázquez-García, Synthesis, optical, electrochemical, and magnetic properties of new ferrocenyl chalcone semiconductors for optoelectronic applications, J. Mater. Sci. Mater. Electron. 31 (2020) 3342–3353, https://doi.org/10.1007/s10854-020-02882-1.
[38] D.A. Zainuri, M. Abdullah, M.F. Zaini, H. Bakhtiar, S. Arshad, I. Abdul Razak, Fused ring effect on optical nonlinearity and structure property relationship of anthracenyl chalcone based push-pull chromophores, PloS One 16 (2021) e0257808, https://doi.org/10.1371/journal.pone.0257808.
[39] A. Saha, Nonlinear optical properties of chalcone derivatives-a short review, Mater. Today Proc. 64 (2022) 605–610, https://doi.org/10.1016/j.matpr.2022.05.131.
[40] L.B. Costa, C.A.F.E. Santos, J.E. Queiroz, A.S.N. Aguiar, L.O. Sallum, J.M. F. Custodio, G.L.B. Aquino, A.J. Camargo, C. Valverde, H.B. Napolitano, Synthesis, characterization, and supramolecular analysis of a novel chalcone derivative: exploring nonlinear optical applications, Rendiconti Lincei 35 (2024) 131–147, https://doi.org/10.1007/s12210-024-01238-9.
[41] H. Song, Z. Kuang, X. Wang, Y. Guo, Q. Guo, H. Zhang, A. Xia, Solvent polarity dependent excited state dynamics of 2′-hydroxychalcone derivatives, J. Phys. Chem. C 122 (2018) 15108–15117, https://doi.org/10.1021/acs.jpcc.8b03133.
[42] P. Verma, R. Mathew, N. Dhiman, P.K. Mitra, Y.A. Lakshmanna, Ultrafast excited-state dynamics of 4-hydroxychalcone: role of intramolecular charge transfer and photoacidity, Phys. Chem. Chem. Phys. 27 (2025) 7716–7727, https://doi.org/10.1039/D4CP04525D.
[43] B. Corbin, P. Houglan, Y. Pang, Fluorescence of 2-hydroxy chalcone analogs with extended conjugation: ESIPT vs. ICT pathways, Molecules 29 (2024) 5972, https://doi.org/10.3390/molecules29245972.
[44] L.F. Sciuti, C.H.D. dos Santos, L.H.Z. Cocca, A.G. Pelosi, R.G.M. da Costa, J. Limberger, C.R. Mendonça, L. De Boni, Studying the first order hyperpolarizability spectra in chalcone-based derivatives and the relation with one- and two-photon absorption transitions, J. Chem. Phys. 159 (2023), https://doi.org/10.1063/5.0166036.
[45] S. Kumar Panigrahi, A. Kumar Mishra, Inner filter effect in fluorescence spectroscopy: as a problem and as a solution, J. Photochem. Photobiol. C Photchem. Rev. 41 (2019) 100318, https://doi.org/10.1016/j.jphotochemrev.2019.100318.
[46] M.J. Frisch, G.W. Trucks, H.B. Schlegel, G.E. Scuseria, M.A. Robb, J.R. Cheeseman, G. Scalmani, V. Barone, G.A. Petersson, H. Nakatsuji, X. Li, M. Caricato, A. V. Marenich, J. Bloino, B.G. Janesko, R. Gomperts, B. Mennucci, H.P. Hratchian, J. V. Ortiz, A.F. Izmaylov, J.L. Sonnenberg, D. Williams-Young, F. Ding, F. Lipparini, F. Egidi, J. Goings, B. Peng, A. Petrone, T. Henderson, D. Ranasinghe, V. G. Zakrzewski, J. Gao, N. Rega, G. Zheng, W. Liang, M. Hada, M. Ehara, K. Toyota, R. Fukuda, J. Hasegawa, M. Ishida, T. Nakajima, Y. Honda, O. Kitao, H. Nakai, T. Vreven, K. Throssell, J.A. Montgomery Jr., J.E. Peralta, F. Ogliaro, M. J. Bearpark, J.J. Heyd, E.N. Brothers, K.N. Kudin, V.N. Staroverov, T.A. Keith, R. Kobayashi, J. Normand, K. Raghavachari, A.P. Rendell, J.C. Burant, S.S. Iyengar, J. Tomasi, M. Cossi, J.M. Millam, M. Klene, C. Adamo, R. Cammi, J.W. Ochterski, R.L. Martin, K. Morokuma, O. Farkas, J.B. Foresman, D.J. Fox, Gaussian 16 Revision C.01 2024, 2016.
[47] Shipra Baluja, Nayan Vakariya, Anchal Kulsheshth, Thermal analysis of some novel chalcones, Journal of Progressive Research in Chemistry [JPRC] 5 (2017) 211–216.
[48] D.S. Manoel, A.G. Pelosi, L.H. Zucolotto Cocca, G.F.B. Almeida, L.F. Sciuti, R.D. F. Rodriguez, L. Adriano Junior, R.S. Lima, C. Noda-Perez, F.T. Martins, M.A. R. Souza, P.J. Gonçalves, T.L. Fonseca, L. de Boni, C.R. Mendonça, Second- and third-order nonlinear optical properties of mono-substituted terpenoid-like chalcones, J. Photochem. Photobiol. A Chem. 429 (2022) 113898, https://doi.org/10.1016/j.jphotochem.2022.113898.
[49] R. Kumari, A. Varghese, L. George, S. Y. N., Effect of solvent polarity on the photophysical properties of chalcone derivatives, RSC Adv. 7 (2017) 24204–24214, https://doi.org/10.1039/C7RA01705G.
[50] N.B. Marucci, J.V.P. Valverde, G. de O. Campos, E.S.A. Ducas, P.J. Gonçalves, L. De Boni, C.R. Mendonça, Two-photon absorption and dynamics of excited states in bromochalcone derivatives, J. Phys. Chem. A 129 (2025) 9119–9128, https://doi.org/10.1021/acs.jpca.5c02748.
[51] M.J. Kamlet, J.L.M. Abboud, M.H. Abraham, R.W. Taft, Linear solvation energy relationships. 23. A comprehensive collection of the solvatochromic parameters, . pi.*, .alpha., and .beta., and some methods for simplifying the generalized solvatochromic equation, J. Org. Chem. 48 (1983) 2877–2887, https://doi.org/10.1021/jo00165a018.
[52] P.L. Franzen, L. Misoguti, S.C. Zilio, Hyper-Rayleigh scattering with picosecond pulse trains, Appl. Optics 47 (2008) 1443, https://doi.org/10.1364/AO.47.001443.
[53] J.M.F. Custodio, G.D.C. D'Oliveira, F. Gotardo, L.H.Z. Cocca, L. de Boni, C.N. Perez, H.B. Napolitano, F.A.P. Osorio, C. Valverde, Second-order nonlinear optical properties of two chalcone derivatives: insights from sum-over-states, Phys. Chem. Chem. Phys. 23 (2021) 6128–6140, https://doi.org/10.1039/d0cp06469f.
[54] J.M.F. Custodio, G.D.C. D'Oliveira, F. Gotardo, L.H.Z. Cocca, L. De Boni, C.N. Perez, L.J.Q. Maia, C. Valverde, F.A.P. Osório, H.B. Napolitano, Chalcone as potential nonlinear optical material: a combined theoretical, structural, and spectroscopic study, J. Phys. Chem. C 123 (2019) 5931–5941, https://doi.org/10.1021/acs.jpcc.9b01063.
[55] L.R. Dalton, P.A. Sullivan, D.H. Bale, Electric field poled organic electro-optic materials: state of the art and future prospects, Chem. Rev. 110 (2010) 25–55, https://doi.org/10.1021/cr9000429.

[56] D.M. Burland, R.D. Miller, C.A. Walsh, Second-order nonlinearity in poled-polymer systems, Chem. Rev. 94 (1994) 31–75, https://doi.org/10.1021/cr00025a002.
[57] G.J. Ashwell, Langmuir-Blodgett films: molecular engineering of non-centrosymmetric structures for second-order nonlinear optical applications, J. Mater. Chem. 9 (1999) 1991–2003, https://doi.org/10.1039/a902604e.
[58] E. Cariati, M. Pizzotti, D. Roberto, F. Tessore, R. Ugo, Coordination and organometallic compounds and inorganic–organic hybrid crystalline materials for second-order non-linear optics, Coord. Chem. Rev. 250 (2006) 1210–1233, https://doi.org/10.1016/j.ccr.2005.09.013.
[59] P.J. Campagnola, L.M. Loew, Second-harmonic imaging microscopy for visualizing biomolecular arrays in cells, tissues and organisms, Nat. Biotechnol. 21 (2003) 1356–1360, https://doi.org/10.1038/nbt894.